# REPORT DOCUMENTATION PAGE

| 1. REPORT DATE *(30-12-2011)* | 2. REPORT TYPE Final | 3. DATES COVERED *(From - To)* 01 May 10–30 Apr. 11 |
|---|---|---|

**4. TITLE AND SUBTITLE**

Multi-scale modeling of novel Hall thrusters: understanding physics of CHT and DCF Thrusters

**5a. CONTRACT NUMBER**

**5b. GRANT NUMBER**
FA9550-10-1-0188

**5c. PROGRAM ELEMENT NUMBER**

**6. AUTHOR(S)**
Michael Keidar

**5d. PROJECT NUMBER**

**5e. TASK NUMBER**

**5f. WORK UNIT NUMBER**

**7. PERFORMING ORGANIZATION NAME(S) AND ADDRESS(ES)**

George Washington University

**8. PERFORMING ORGANIZATION REPORT NUMBER**

**9. SPONSORING / MONITORING AGENCY NAME(S) AND ADDRESS(ES)**
AFOSR, Dr. Mitat Birkan
Air Force Office of Scientific Research
875 North Randolph St.
Arlington, VA 22203

**10. SPONSOR/MONITOR'S ACRONYM(S)**

**11. SPONSOR/MONITOR'S REPORT NUMBER(S)**
AFRL-OSR-VA-TR-2012-0779

**12. DISTRIBUTION / AVAILABILITY STATEMENT**

Distribution A

**13. SUPPLEMENTARY NOTES**

**14. ABSTRACT**
In order to simulate the magnetized plasma thruster devices (such as CHT, DCF etc) we have developed a
multi-scale numerical code that is based on coupling of a PIC/MCC analysis of neutrals and ions in a
general 2D domain (or 3D) and a 1D kinetic full PIC treatment of electrons along magnetic fields. The
implementation of such a two-way coupling allows calculation of the electron transport in the real
physical domain while significantly reducing the computational time associated with 2D full kinetic
simulations. The objective of this study was to identify the individual contribution to transport from factors
such as collisions, surface roughness, secondary electron emission, and plasma oscillations.
Multi-scale model of the magnetized plasma thruster discharge in which a kinetic treatment was used for the electron component while a
2D (or 3D) macroscopic model will be employed for ion and neutral component analysis. Initial coupling of the
microscopic and macroscopic model was performed via axial electric field, electron fluxes to the wall
and electron cross-field transport. This model demonstrated improved prediction of electron mobility.

**15. SUBJECT TERMS**

| 16. SECURITY CLASSIFICATION OF: | | | 17. LIMITATION OF ABSTRACT | 18. NUMBER OF PAGES | 19a. NAME OF RESPONSIBLE PERSON |
|---|---|---|---|---|---|
| a. REPORT | b. ABSTRACT | c. THIS PAGE | | | 19b. TELEPHONE NUMBER *(include area code)* |

# Multi-scale modeling of novel Hall thrusters: understanding physics of CHT and DCF thrusters

Michael Keidar

Department of Mechanical and Aerospace Engineering

The George Washington University, Washington DC

Final Report

# Abstract

In order to simulate the magnetized plasma thruster devices (such as CHT, DCF etc) we have developed a multi-scale numerical code that is based on coupling of a PIC/MCC analysis of neutrals and ions in a general 2D domain (or 3D) and a 1D kinetic full PIC treatment of electrons along magnetic fields. The implementation of such a two-way coupling allows calculation of the electron transport in the real physical domain while significantly reducing the computational time associated with 2D full kinetic

simulations. The objective of this study was to identify the individual contribution to transport from factors such as collisions, surface roughness, secondary electron emission, and plasma oscillations. Multi-scale model of the magnetized plasma thruster discharge in which a kinetic treatment was used for the electron component while a 2D (or 3D) macroscopic model will be employed for ion and neutral component analysis. Initial coupling of the microscopic and macroscopic model was performed via axial electric field, electron fluxes to the wall and electron cross-field transport. This model demonstrated improved prediction of electron mobility.

# Section 1, Multiscale Modeling of Hall Thrusters

## Introduction

Despite Hall thrusters having over 40 years of flight heritage (the first variant, SPT-50, was flown aboard the Soviet Meteor spacecraft in 1971), the community still lacks a tool capable of predictively modeling these devices. The closest to an industry standard, COTS-level simulation program is HPHall. This 2D axisymmetric code was originally developed at MIT by Fife,[1] and was subsequently improved by others.[2, 3] Other researchers have developed their own codes based on the basic premise of HPHall.[4–7] These codes share a common approach. Ions are treated as kinetic particles while electrons are modeled as a quasi-1D fluid. Quasineutrality is assumed, and the kinetically determined plasma density is used to update the electron temperature in direction perpendicular to the magnetic field lines. Potential is recovered by considering current conservation and assuming electron thermalization along field lines. This model is generally valid - in Hall thrusters electrons are magnetized, and thus their motion can be decoupled into two distinct modes: the unhindered motion along the field line, and the mobility-driven diffusion across them. The mobility term comes into play in the electron momentum equation used to determine the cross-field velocity. This is one of the terms in the energy equation. HPHall relies on the classical $1/B^2$ collision driven transport combined with an anomalous $1/B$ Bohm term. Mathematically, the mobility model is $\mu_{e,\tilde{n}} = \mu_e /(1+ \beta^2) + K_b /(16B)$, where $\mu_e$ is the mobility $\mu_e = e/\nu_{en} m_e$ for unmagnetized electrons, $K_b$ is the user-determined Bohm parameter and $\beta = \omega_c /\nu$ is the Hall parameter. This formulation is not without problems. Transport is inherently a kinetic phenomenon. It is influenced to a large degree by wall collisions, secondary electron emissions, and temporal field variations. These are kinetic effects that the simple analytical model fails to capture. In addition, as pointed out previously by Sydorenko,[8] electron temperature in Hall thrusters is anisotropic, further complicating the model.

Hence, several other researchers have taken path completely opposite of HPHall, and have developed fully kinetic Hall thruster codes. Example of one such code is the work of Hirakawa.[9] Many other researchers have also contributed.[10–12] These fully kinetic codes have their own drawbacks. First, they require extremely small simulation time steps. Resolving the cyclotron rotation requires timesteps some six orders of magnitude smaller than required to push ions in HPHall. Second, since potential in these codes is obtained from solution of the Poisson's equation, the computational cells must be small enough to resolve the Debye length. These two requirements make fully kinetic approach a computationally daunting task for all but the smallest of thrusters. Even if tricks are played with relative electron-to-ion mass and the free space permittivity, these codes still require supercomputers and many days or weeks of computational effort.

Fully kinetic codes are useful tools for understanding basic physical processes occurring in Hall thrusters. They are not particularly useful, however, to a designer working on optimizing one of these devices. Designer at some aerospace corporation will likely not have access to supercomputing facilities, nor have the time to perform a trade study if each cases requires substantial computational effort. For this reason, we started working on a new multiscale approach to modeling Hall thrusters. The objective of our work is to develop a tool capable of self-consistently determining electron mobility and the thruster plasma properties of interest, but do it in such a way that a solution can be obtained on a standard desktop workstation in less than a day. To accomplish this goal, we divide the problem into the following three spatial scales:

- **Magnetic Field Line:** On the spatial scale of a magnetic field lines, dynamics is driven by the cyclotron motion of electrons. Electrons are magnetized, and individual field lines can be

considered independent of each other. Heavy particle and properties normal to the field lines are assumed frozen. This approach allows us to rapidly simulate electrons and recover mobility self-consistently. Leveraging modern multi- core architectures via multithreading allows us to study multiple field lines simultaneously.

- **Thruster Channel:** On the spatial scale of the thruster, plasma is assumed to be quasineutral, and electron density can be obtained from kinetic ions. Electron temperature and plasma potential is obtained by solving the quasi-1D equations. This approach is identical to HPHall, except that our method relies on the mobility determined by the kinetic analysis. Ions exiting the thruster at steady state are sampled to obtain a discretized source term for plume modeling.

- **Plume Environment:** Outside the thruster exit, the magnetic field plays a negligible role. The plume is quasineutral except in low density sheath regions around the spacecraft. Of interest here is the formation of charge exchange ions and their impact on spacecraft components. Electron density is obtained from Boltzmann relationship, and potential can be solved by direct inversion or by solving Poisson's equation.
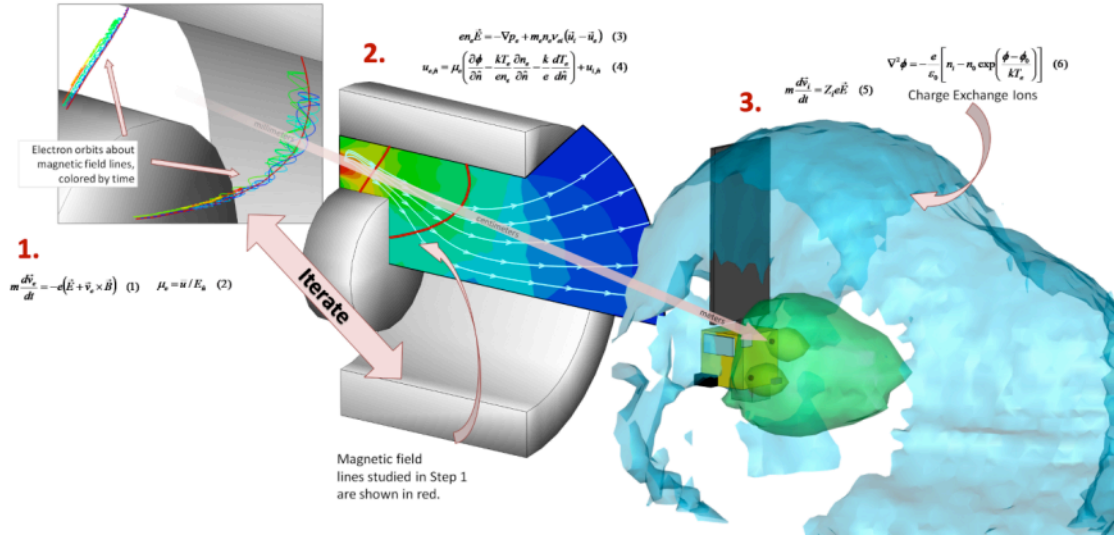


*Figure 1. Schematic of our multiscale approach. Codes 1. and 2. are designed to iterate until convergence. We then sample ions crossing the thruster exit plane to obtain the source model for plume analysis.*

This approach is shown schematically in Figure 1. This formulation naturally lends itself to three codes, each concentrating on the physics of the respective spatial scale. The first code, Lynx, simulates the cyclotron motion of electrons about series of magnetic field lines. The second code, a general 2D axisymmetric / Cartesian plasma simulation tool Starfish, is still in development, and hence in this paper we utilized HPHall. The final piece is the 3D plume code Draco. We begin the paper by describing the thruster to which this approach was applied. We next skip to the second step, and use HPHall to obtain the initial plasma parameters which will serve as inputs to Lynx. We then perform a kinetic analysis to compute new values mobility. These are then used to update the HPHall solution and extract the plume source model. Repetitive iteration between steps 1 and 2 is left as a future item that will be attempted once Starfish development is complete. The paper concludes with a summary and a discussion of future work.

## Thruster Details

We deploy our model to the 2.6cm Princeton Cylindrical Hall thruster (CHT). This thruster is described in greater detail in Ref. 13. Here we summarize just the parameters important to our analysis. The most important characteristic of this device is its non-standard geometry. While typical Hall thrusters consist of an annular channel, the CHT contains an annular upstream zone and a cylindrical acceleration zone. The lack of the inner wall in the acceleration region is expected to lead to an increased thruster lifetime and improved performance due to reduced losses of ions to the walls. From the academic standpoint, this configuration also introduces interesting new physics. The magnetic field lines converge near the innerpole, resulting in a region of increased magnetic pressure. Electrons are then expected to be preferentially scattered to the outer wall, possibly resulting in a non-symmetric sheath. This finding was touched upon in our previous work.[14]

The walls of this SPT-type thruster are made of a dielectric material. The dielectric walls distinguish this thruster design from another Hall thruster variant, TAL (thruster with anode layer), in which the walls are conductive. One theory of SPT operation suggests that electron impacts of the dielectric material result in emission of secondary electrons from the material matrix. Since these electrons are not initially magnetized, they are free to migrate towards the anode. This theory is called near wall conductivity (NWC) and it's a feature that is captured by our kinetic code. These electrons are also significantly colder than the impacting particles, resulting in the cooling of the primary population.

Experimental measurements of this thruster have been presented in Refs. 15 and 16. The CHT can be operated in two modes based on the current applied to the magnetic coils. Our work correlates to the "direct" mode. In this configuration, magnetic field lines cross the channel between the outer wall and the innnerpole without forming a cusp near the outer wall. Electron temperature in the thruster was found to peak at 25 eV just outside the exit plane. Potential decays slowly through majority of the channel. Only 50V of potential drop were measured in the first 1.5cm from the anode. Most of the potential drop occurs near the exit plane, in the acceleration zone. Additional 50V potential drop was measured to occur outside the thruster. Anode current was approximately 0.3A, and plasma density was $\sim 6 \times 10^{17} \, \text{m}^3$.

## Initial Results for Thruster Discharge

We used the HPHall simulation code to model the discharge channel. Schematic of our setup is shown in Figure 2. HPHall uses a structured but non-uniform mesh, boundary of which is shown in the figure. Such a mesh simplifies capturing the geometry of non-rectangular devices, as well as the downstream near-plume region. Internally, HPHall establishes another virtual mesh that is used to solve the electron equations. This mesh is illustrated in Figure 2. The vertical lines correspond to approximately equidistantly spaced magnetic field $\lambda$ lines. It should be noted that this graphics does not completely correlate to the implementation in HPHall. The data structure used internally by the code uses a variable number of radial segments, which leads to a more complicated visualization problem. The mesh shown here, and in our subsequent analysis, used a uniform number of radial segments corresponding to the average number used by HPHall.

Of importance are the left and the right boundaries. These correspond to the anode and the cathode, respectively. Constant potential is applied upstream of the anode. The anode potential is computed by the code self consistently. The right boundary is the cathode line on which potential, density, and temperature are specified. Simple linear interpolation for temperature and potential is used downstream of the cathode. As can be seen from the figure, this downstream region can encompass a substantial fraction of the simulation domain. Important part of setting up an HPHall simulation is

determining where to place the anode and the cathode lines. Typically, trade study is performed and the solution in the best agreement with experiments is selected.
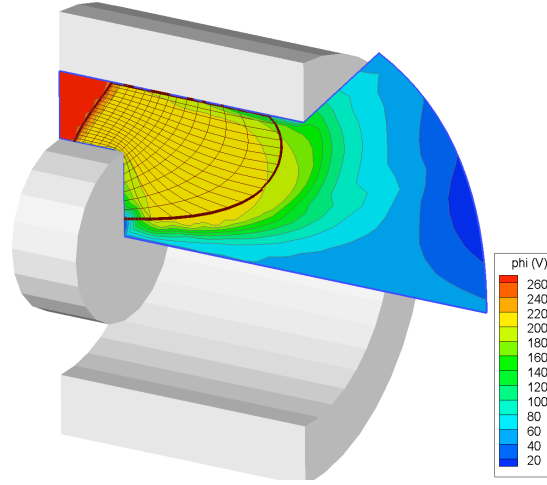


*Figure 2. Simulation model of the cylindrical Hall thruster. Slice shows the HPHall computational domain. The mesh corresponds to the region in which the electron conservation equations are solved.*

HPHall injects kinetic electrons at the anode. Ionization model is then used to create ion particles. Ion positions are integrated using the particle in cell method. The code assumes charge neutrality, and hence $n_e = n_i + 2n_{i2}$ , summation of singly and doubly charged ion populations. In order for quasineutrality

to hold, electron temperatures must adjust accordingly to accommodate diffusion. HPHall solves the energy equation

$$\frac{\partial}{\partial t}\left(\frac{3}{2}kT_e\right) + \nabla \cdot \left(\frac{3}{2}n_e kT_e \vec{u} + \vec{q}_e\right) + \nabla \cdot (n_e kT_e \vec{u}_e) = S_h - S_i \tag{1}$$

on the previously described lambda mesh. Constant electron temperature at each field line is assumed. This then allows each field line to be treated as a single volume element. Relevant properties, such as mobilities or electron densities, are integrated along the line following the standard finite volume formulation. In other words, the computation is performed in a quasi-1D dimension. The conservation equations are solved only in the direction normal to the field lines, but 2D radial contribution is used to compute the coefficients at each point. Electron velocity, given by the momentum balance,

$$\vec{u}_e = \mu_e \left(\frac{d\phi^*}{d\hat{n}} + \frac{k}{e}(\ln(n_e) - 1)\frac{dT_e}{d\hat{n}}\right) + u_i \tag{2}$$

is incorporated into the temperature solver. Here $\mu_e$ is the mobility term. Once temperature has been

determined, the thermalized potential $\varphi$ can be computed at each lambda line from current conservation. The radial variation in potential is then recovered from the thermalized potential relationship, $\phi^* = \phi - kT_e/e\ln(n_e)$.

In our previous work[14] we performed a limited parametric study where we investigate several different cathode line positions and Bohm parameters with the goal of matching the experimental measurements for CHT. We were able to improve our correlation for this work. The relevant input settings are summarized in Table 1. Plasma properties along the thruster centerline are plotted in Figure 6. This figure shows both the results obtained using the analytical mobility model, and the results obtained subsequently using our kinetic method. The initial results with the analytical mobility are plotted with dashed lines. It should be noted that there are still discrepancies. For one, the HPHall-predicted potential distribution fails to capture the gradual rise to the anode potential. Instead, potential is actually seen to decrease upstream of the start of the acceleration zone. This indicates that fraction of ions born in this regions will have the tendency to flow towards the anode. One of the goals for this work was to determine if any improvement can be achieved by modifying the mobility distribution using the kinetic code.
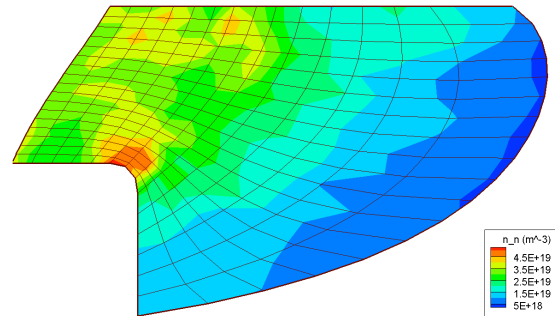
## Kinetic Code Inputs

The kinetic code requires as inputs information related to the global state of the discharge. We developed a simple code to contour HPHall results (`2d_ave_tp.dat`) along the lambda lines for computation. Contouring starts by searching for the corresponding value along the bottom edge of the computational domain. Edge cuts are then determined by linear interpolation of node values, and the cuts are connected to form a spline. Properties of interest are then interpolated onto the spline control points. Figure 3 shows the parameters. Along with the magnetic field profile (not shown here), these five parameters serve as inputs to the kinetic code. The kinetic code is described in the next section.

*Table 1. Summary of critical inputs for the HPHall simulation*

| Parameter | Value |
|---:|:---|
| Mass flow rate | $4 \times 10{-7}$ (kg/s) |
| Discharge voltage | 275 V |
| Anode line position | (0.0520, 0.010) m |
| Cathode line position | (0.0670, 0.010) m |
| Cathode temperature | 26 eV |
| Cathode potential | 210.6 V |
| Cathode density | $\times 10^{17}$ m$^{-3}$ |
| Cathode emitter potential | -20 V |
| Bohm coefficient | 1 |
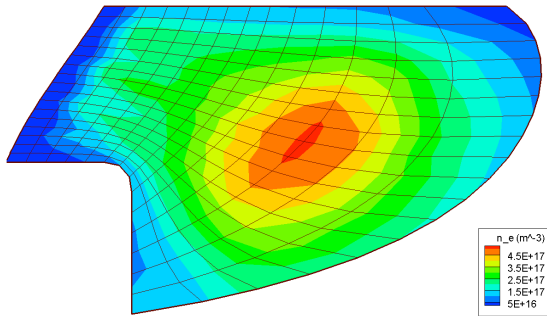


(a) Plasma Density



(b) Neutral Density
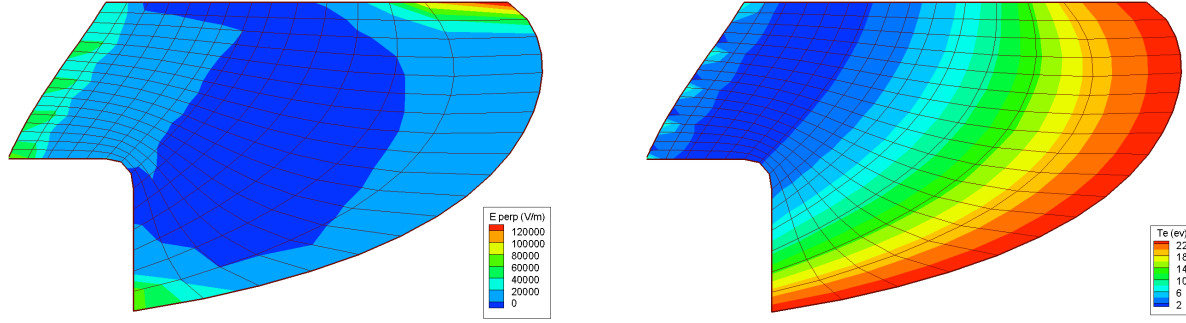
(c) Normal Component of Electric Field      (d) Electron Temperature

*Figure 3. Plasma parameters serving as inputs to the kinetic code. Kinetic simulation is performed for each field line (vertical grid lines). Additional input, which is not shown here, is the magnetic field strength.*

## Mobility Calculation with Lynx

The inputs in Figure 3 are next processed with a kinetic code called Lynx. Lynx is a kinetic code that self-consistently calculates the radial variation in electron mobility along a magnetic field line.[14, 17] Lynx simulates only electrons. Ions and neutrals are assumed to remain frozen during the time necessary to compute electron trajectories. The heavy particles thus form a fixed background with which the electrons interact during their cyclotron motion about the field line. By repeating the calculation for all the lambda lines making up the HPHall electron mesh, we can obtain a two-dimensional variation in mobility. This kinetically determined mobility can then be used in HPHall in lieu of the analytical model.

Lynx is implemented in Java. Although historically Java performance was not competitive with languages such as C/C++, this is no longer the case. Modern Java compilers generate codes that perform at speeds comparable and in some cases even exceeding native C++ implementation.18 In addition, Java offers a large standard library with support for data management, as well as GUI, networking, and graphics rendering. In addition, Java natively supports multithreading which allows us to take advantage of modern multi-core system architectures, and run Lynx concurrently for multiple field lines.[19] Similar functionality can be achieved in C++ through the Boost libraries. However, that step requires downloading, configuring, and compiling the massive libraries. In Java, such support is provided natively.

## A. Execution and Topology

Lynx simulation commences with the code importing the 2D mesh shown previously in Figure 3. An additional settings file is also processed. This settings file specifies general simulation parameters such as wall temperature, number of electrons per field line, and the number of time steps. It also controls which diffusion-inducing processes, such as collisions or wall effects should be included. Lynx next instantiates a new simulation object for each magnetic field line. A simple scheduler was implemented to launch the threads and monitor them for completion. The number of threads running concurrently is limited by the number of available CPU cores.

The computational domain for each Lynx simulation thread is a one dimensional domain corresponding to a particular lambda line. In Figure 3, each vertical grid line corresponds to an individual simulation. The number of nodes along the line differed from the coarse mesh shown in this figure and was determined automatically such that $\Delta s = 0.5\lambda D$ . On average, 100 nodes were used per magnetic field line. Note, the coarse input mesh was used to store transport properties. The coarser mesh was selected in order to reduce statistical noise errors. Several fixed properties are set at each grid node during the initialization. These

include ni and n0 , ion and neutral densities, E , perpendicular component of electric field, B, magnetic field strength, and $\partial B/\partial s$, magnetic field gradient.

## B. Particle Loading

The simulation then continues by loading the electron particles. Electrons are loaded at grid nodes, with the number of electrons obtained by multiplying the ion density by cell volume and scaling by the particle weight. As pointed out by Fox,[11] careful sampling of electrons is necessary in order to resolve the high energy tail of the velocity distribution function. We did not take this approach at this time, but plan to investigate the effect of variable particle weight on transport and near wall conductivity in the near future. The initial electron temperature at each field line is one of the inputs from HPHall. Isotropic temperature distribution was used for particle loading. Particles are loaded such that the axial position of the guiding center is z = 0. Initial number of particles was 50,000.

The initial plasma sheath profile needs to be determined next. Since ions are frozen, the establishment of equilibrium sheath is marked by zero electron current to the walls. During this initial period, collisions were not performed, and secondary electrons were not emitted. Instead, particles impacting the walls were simply removed from the simulation domain. These processes were ignored since we are interested in determining the electron density distribution arising from the thermal and potential balance. In our simulations, we found that steady state was achieved after approximately 1500 time steps. However, for an added margin of safety, we required to code to complete 3000 steps before the simulation continued. The additional time steps have no impact on the results since once the steady state is achieved, electrons become trapped in the potential well between the walls and are unable to reach the walls.

Simulation then moves to the normal operating mode, with collisions and SEE turned on. Particles translating away from the field line, or impacting the walls were removed from the simulation. The code reinjected new particles into the simulation to keep the number of electrons at the steady state level. Total of 20,000 time steps were simulated. Averaging of results began at time step 5000. The intermediate period between steady state and averaging was excluded from averaging to avoid any possible initial transient effects from influencing the results. The timestep $\Delta t$ was selected such that electrons completed single orbit in 75 time steps.

## C. Collisions and Near Wall Conductivity

Electron collisions were modeled using the Monte Carlo method. In this method, source particles are collided with a stationary target cloud. The collision probability is determined from the background density, n0 and collision frequency is $P = 1 - exp(-n_0\,\sigma_0\,g\Delta t)$ Here $\sigma_0$ is the total collision cross-

section due to all processes. For particles undergoing collision, the collision process was picked randomly according to the ratio of $\sigma_i\,/\sigma_0$. Post-collision velocity was computed by first sampling a random target

velocity and a random impact angle. We then calculated the post-collision velocity from conservation of energy.

To reduce statistical errors and improve performance, collisions were computed only once every 4 timesteps. Three types of collisions were considered: momentum-transfer (electron-atom), ionization (electron-atom), and excitation (electron-atom). Coulomb collisions were not included in the present work. At low electron temperatures, polarization collisions dominate the momentum-transfer interaction between electrons and atoms.[20] Cross-section for this process was obtained from the analytical model[20]

$$\sigma_{Xe} = \left( \frac{\phi \alpha_p q^2}{\epsilon_0 m} \right)^{1/2} \frac{1}{v} \tag{3}$$

where $\alpha r$ is the polarizability of the atom. It is given by $\alpha r = 27.66a3$ , where $a_0$ is the Bohr radius.[21] Cross-section for electron-ion collisions was given by

$$\sigma_{Xe^+} = \frac{8}{\pi} b_0^2 \ln\Lambda \tag{4}$$

where $b_0 = q_1 q_2 /(2\pi\epsilon_0\, mv^2\,)$ is the distance of closest approach. The inelastic process, ionization and

ex- citation, cross-sections were computed using the polynomial fit of Szabo.[22]   These collisions were modeled by reducing the energy of the impacting electron by the ionization or excitation energy, and scattering the electron through a random angle.

Electrons impacting the dielectric walls were reflected back to the domain, absorbed, or generated secondary electrons according to the model of Sydorenko.[23]  The secondary electron yield was given by,

$$\gamma = \left( \frac{E_p}{35eV} \right)^{0.5} \tag{5}$$

The SEE yield is non-negligible for $kT_e = 10eV$. The SEE electrons were assumed to come off the surface unmagnetized, and were generated at the wall with initial direction given by a random velocity vector. Impacting electron knocking off a secondary electron was assumed to be absorbed by the wall to retain charge neutrality, and was removed from the simulation. Although we have implemented a simple analytical model to take into account surface charging of dielectric walls, we did not utilize it at present. Instead, potential was fixed at both walls at 0V.

Figure 4 shows the typical field line quantities. This particular plot was generated for a magnetic field line close to the anode. We can see that in the bulk region, electrons clearly follow the ions. This charge neutrality is captured by the potential solution, leading to zero electric field in this bulk region.  A clear sheath forms near the walls. Electron density decays faster, as expected. Electric field forms near the walls to repel low energy electrons. Wall potential drop is   5.7kTe.

## D. Transport Calculation

Previous paragraphs described the methods used to simulate magnetized electrons bounded between two walls. In order to make the model useful to our multiscale approach, we need to extract mobility from the solution. Conceptually, determining mobility is a trivial task. Mobility could be obtained as $\mu_j = \Sigma u_z / E_\perp$ where $j$ corresponds to a mesh cell, and the sum is performed over all particles in that

cell. Unfortunately, this approach is not feasible numerically. To see why, let's consider the typical values of drift velocity $v_d$ and the tangential velocity of electrons orbiting a field line, $v_T$ . Using values typical of the CHT, $v_d \equiv \mu E = 5m^2 /Vs \times 20,000V/m = 10^5\, m/s$. The tangential velocity can be

approximated as $v_T = \sqrt{kTe/m} = 10^6$ m/s. From this simple calculation, we can see that $v_T > v_d$.

Given a finite number of particles, and the fact the particles translate along the field line during their orbit, the summation will always result in non-zero mobility. Due to the magnitude of $v_T$, a single unpaired term will likely wash out any actual drift velocity.

This shortcoming became obvious during our validation tests. We ran the simulation for a case in which all diffusion terms were disabled, yet the code predicted finite transport. Even more interesting was the fact that mobility was only slightly increased when collisions were included or when electric field was doubled. Hence, we implemented an alternative method of computing drift velocity. Instead of summing the axial components of particle velocity, we consider the velocity of the guiding center. We determine the guiding center as $r_g = 0.5(z^+ + z^-)$, where $z^+$ and $z^-$ are the extents of particle's position during an orbit. These quantities are reset once per orbit. Drift velocity is then $v_d = r_g/\tau$, where $\tau$ is the time delta since previous sampling.
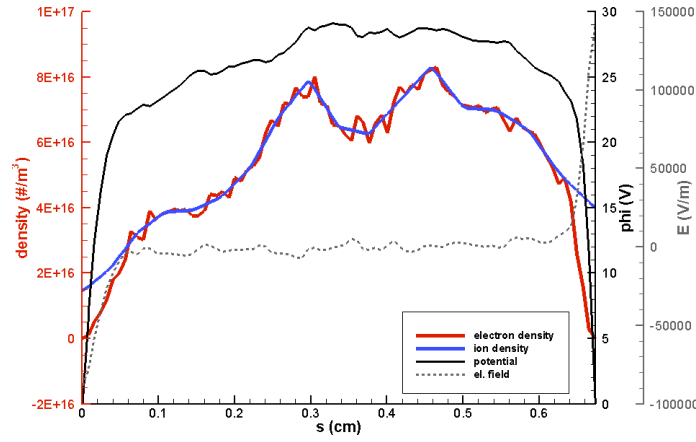


*Figure 4. Plot of typical simulation results. Electrons are seen to closely follow the prescribed ion density, except in the sheath region, where they density decays more rapidly as expected. Plasma potential and tangential electric field profiles are also shown.*

Only particles having diffused more than $1.5r_L$ were counted. Here $r_L$ is the local Larmor radius computed using particle's tangential velocity, and the strength of the magnetic field at the particle location. Stray particles were removed from the simulation and were subsequently replaced by new particles at the field line. The radial position of the newly created particles was based on the density of the ions.

All simulations presented in this paper were executed on a Sony VAIO laptop with the Intel Core i7 2.5GHz CPU. This CPU supports up to 8 concurrent threads. Typical simulation times ranged from 400 seconds for a quick estimate with 10,000 particles and 10,000 time steps to 2600 seconds for the runs used to generate the results for this paper. These runs used 50,000 particles and ran for 20,000 time steps. Computed properties, including mobility, were then exported as a 2D mesh.

Figure 5 compares the mobility computed using our kinetic approach to that used by HPHall. Although the background values of mobility are similar quantitatively, we can see stark differences between the two versions. The kinetic solution contains two distinct regions of high mobility which are not seen in the analytical model. High production of secondary electrons was predicted by the code for the field lines at the left band. NWC may also explain the oscillatory nature of transport, which seems to be related to the high number of SEE seen on the magnetic field lines in this region. On the

other hand, the high mobility in the right band may be due to a strong electric field. The right field line corresponds to the location where HPHall predicts drop in potential corresponding the the start of the acceleration zone. We also see reduced mobility near the innerpole. This region is dominated by increased magnetic pressure which reduces flux of electrons to this region. It should be noted that the results shown here are statistically accurate. We performed multiple simulations with a varying number of particles, and all simulations produced comparable results.
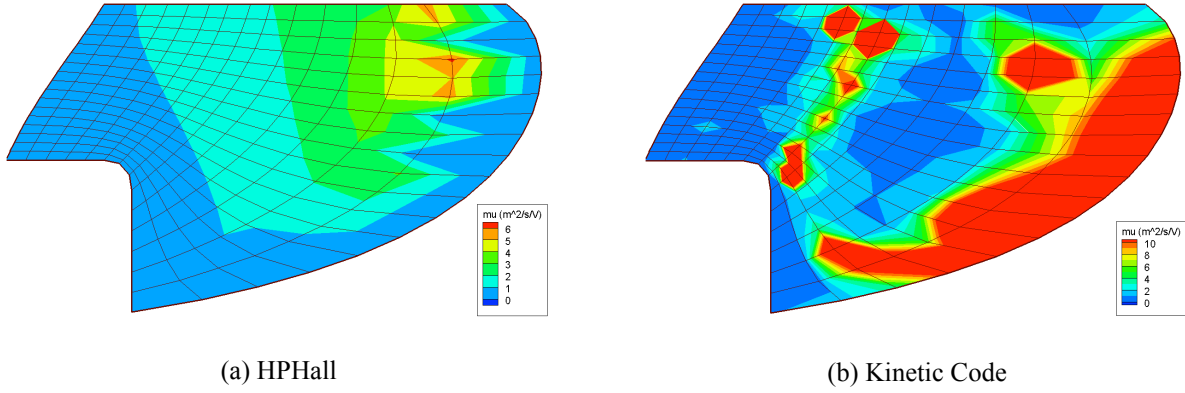


(a) HPHall                 (b) Kinetic Code

*Figure 5. Comparison of the analytical mobility used by HPHall (left) to the kinetically determined mobility from Lynx.*

## HPHall results with kinetic mobility

The mobility contour obtained in Lynx was next loaded into HPHall. We modified HPHall to load mobility values from a file. We next ran HPHall for 5,000 time steps, and exported the new 2D results. Comparison of centerline plasma properties can be seen in Figure 6. Solid markers correspond to experimental data. The dashed lines are the results obtained with the classical model, and the solid lines are the ones obtained by loading the self-consistently determined mobility. A clear improvement in plasma potential is seen. Although the potential deviates somewhat from the control point, the potential is seen to increase towards the anode, and the trough region is eliminated. Temperature results are less conclusive, partly due to the poor agreement of the initial results with the data. The peak of plasma density is seen to decrease and move towards the anode.
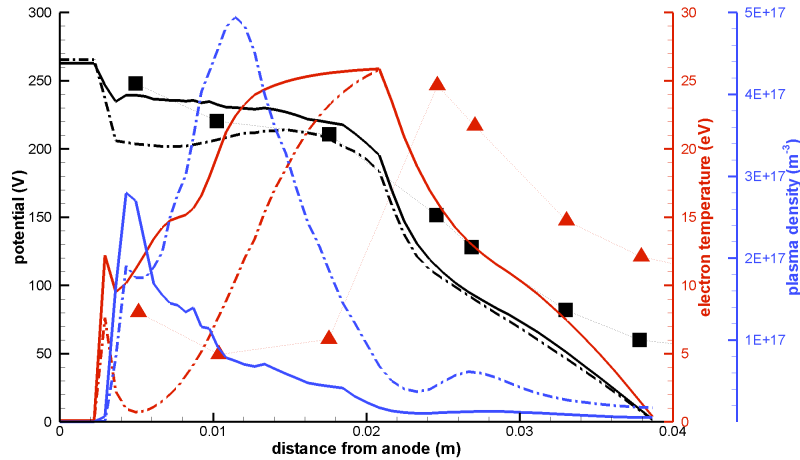
*Figure 6. Plot of several plasma parameters along the thruster centerline. The markers correspond to experimental data from Ref.15 Experimental plasma density, measured in a single point in the channel, was $6 \times 10^{17}$ $m^{-3}$. The results computed using the analytical mobility model are shown using the dashed lines. The results obtained with the kinetic mobility are shown with the solid lines.*

## A. Particle Sampling

During this simulation we also sampled particles crossing a virtual plane in the near plume region. It's difficult to describe the velocity and flux distribution function of the Hall thruster plume analytically. Unlike ion thrusters, Hall thruster discharges are open to the ambient environment, and the acceleration profile is a function of the plume itself. Sampling particles as they cross some plane is a simple and effective way to describe the velocity and flux space. By sampling velocities and the corresponding spatial position for asufficiently large number of particles we can obtain a discretized velocity distribution function. A peculiar feature of Hall thrusters is that some acceleration occurs outside the actual thruster. In the case of the CHT, the external acceleration accounts for approximately 50eV of ion energy. In order to capture this feature, we sample the particles sufficient distance from the exit plane, in a region where potential drop becomes negligible.

## Plume simulations with Draco

The discretized velocity distribution function is next used to model the plume environment produced by these thrusters. The plume modeling was performed using the final piece of our multiscale approach, a 3D ES-PIC code called Draco.[24] Draco was developed at Virginia Tech as a general plasma simulation tool suitable for modeling electric propulsion plumes and their interaction with spacecraft components. It readily interfaces with detailed geometries produced in COTS CAD/CAE packages. The code operates on a rectilinear mesh containing a subset of cut cells. The cut cells are generated automatically based on the user specified geometry surface mesh.

## A. Source Model

Particles are injected into the simulation from source element groups. Draco supports variety of source models, including one developed specifically for interfacing with HPHall.[25] This model takes as its input a file containing a large number of $[r, v_z, v_r, v_\theta]$ tuples. The source randomly selects a tuple from the list and rotates it through a random azimuthal angle $\theta$. Position and and velocity is also rotated according to the normal vector of the source elements. This discretized model offers the benefit of being able to capture not just a general non-Maxwellian velocity distribution space, but also radial variation in mass flux.

## B. Hybrid Potential Solver

Generally two methods exist for obtaining plasma potential for plume simulations. The potential can be obtained by solving the Poisson's equation. This approach requires cell spacing small enough to capture gradients in the solution. Since the plume is quasineutral, and not magnetized, a simpler method is available based on the direct inversion of the Boltzmann relationship for electrons, $\varphi = \varphi_0 + kT_e \ln(n_i / n_0)$. Although this approach computes the correct potential in the plume

region, it does not take into account the non- neutral sheath region. In the case of a GEO satellite, the sheath is not negligible and can expand distances the scale of the spacecraft.

Hence, we implemented a "QN switch" Poisson solver based on the previous work of Santi and Cheng.[26] Prior to commencing the solver iterations, the solver calculates the local Debye length at each node of the simulation domain. If $4/3\pi\lambda^3 < V$, where V is the cell volume, the node is flagged as

quasineutral and potential on it is fixed to the value obtained by the direct inversion. The Poisson solver then backfills the remaining region. Comparison between the two solutions is shown in Figure 7. The plots were generated by injecting particles for a small number of time steps without using any field solver. The simulation was then restarted for zero number of time steps, which resulted in the potential update, but no particle push. Hence, the charge densities are identical. The figure on the left shows the solution obtained by the inversion alone. The figure on the right shows the solution from the Poisson solver with QN-switch. It should be noted that a non-switched Poisson solver was not able to converge for this particular problem. As we can see, the solutions are identical in the plume region, as expected. The QN-switch approach however correctly captures the potential drop outside the negatively charged solar panel. The direct inversion method shown on left effectively compresses the sheath to the thickness given by a simulation cell. The ions are not aware of the solar panel until they reach the cell adjacent to it. This difference has a profound implication on the trajectories of the charge exchange ions, trajectories of which are primarily influenced by the electric fields between the plume and the spacecraft components.



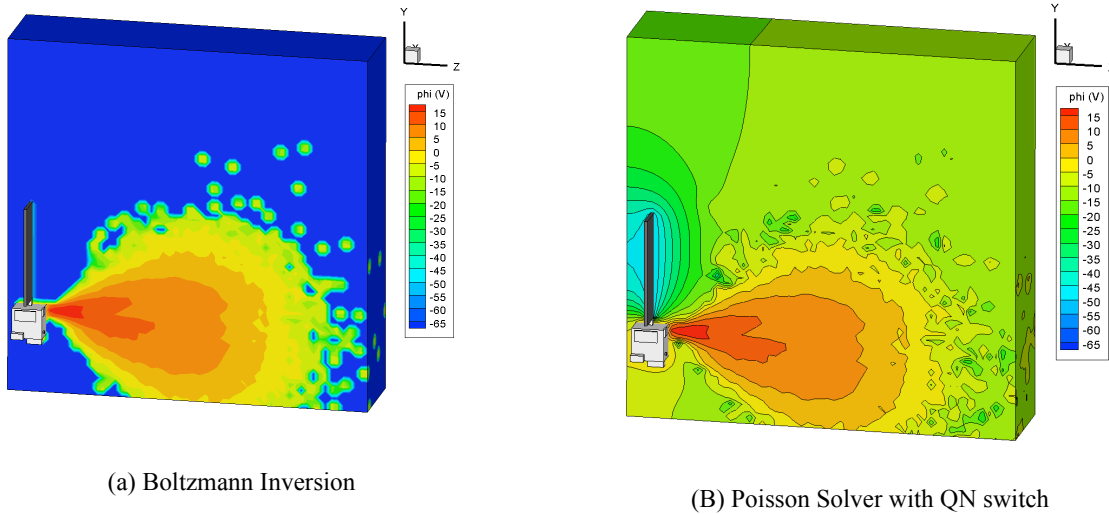(a) Boltzmann Inversion

(B) Poisson Solver with QN switch

*Figure 7. Comparison of electric potential solution for an identical charge density computed using the two approaches. The solution is identical in the plume region, but the QN-switched solver also resolves the sheath around the negatively charged solar panels.*

## C. Plume Results

We used this approach to model the plume environment around a generic spacecraft operating a cluster of two CHT thrusters. The results can be seen in right section of Figure 1. Prominent feature of the spacecraft is a large solar array, which in our model was assumed to float negative in respect to the bus. For simplicity, uniform potential was applied across the solar wing. The potential on the solar array was -20V, and the potential on the bus was 0V. The potential at the thruster exit was 10V. The simulation was performed on a stretched $40 \times 40 \times 46$ mesh. The mesh extended from 8 cm behind the thruster exit plane to 60 cm in front of the thruster. Reference values for the potential solver corresponded to the potential, density, and temperature at the thruster exit. The simulation took approximately 2 hours to complete. An actual detailed analysis of the plume environment produced by this thruster is reserved for future work.

# VII.    Conclusion and Future Work

In this paper we presented a new model for performing multiscale modeling of Hall thrusters. The main feature of our model is its ability to self-consistently determine electron mobility, plasma properties in the thruster channel, and also the plume environment induced by the thruster without relying on supercomputer resources. We demonstrated the approach on the 2.6cm Princeton Cylindrical Hall thruster. Our approach relies on a kinetic code that computes the spatial variation of mobility by considering the cyclotron motion of electrons, a 2D axi-symmetric code for thruster discharge, and a 3D plume code to model the plasma environment and contamination effects.

In this paper we used HPHall to model the thruster discharge. As part of our future work, we plan to perform the thruster modeling using our in-house designed 2D code. Primary motivation for this effort is to simplify the iterative processing needed to obtain a truly self-consistent solution. HPHall is written in C, following non object-oriented procedural implementation. HPHall also contains physics additional to what is needed to capture the thruster plasma environment. The goal for our work is to create a light- weight replacement to HPHall that utilizes modern software engineering paradigms and easily ties in with our kinetic code.
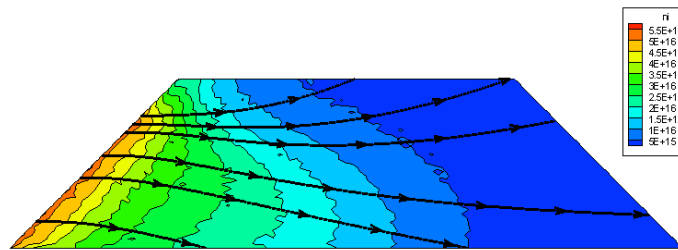


*Figure 8. Plasma density and ion velocity streamlines in the sheath with converging magnetic field lines. The thruster wall forms the upper boundary, and the bottom boundary extends into the quasineutral bulk plasma.*

In addition, we are investigating few additional components of Hall thruster discharge. Modern Hall thrusters, including the CHT, use magnetic fields that intersect the camber walls at off-normal angles. Configurations with highly oblique angles have been proposed to create the so-called magnetic lens, which effectively focuses ions and pushes them away from walls. However, in such a configuration, the radial component of electric field normal to the magnetic field lines can exceed the component due to the sheath drop. In that case, the net electric field points away from the walls, and the sheath collapses. We have developed a code specifically to study this near wall sheath region in highly oblique magnetic fields. A typical solution is shown in 8. The goal of this work is to produce an algebraic model that can be coupled into the thruster code to correctly compute the sheath potential drop.

## References

1.   Fife, J. and Martinez-Sanchez, M., "Two-Dimensional Hybrid Particle-In-Cell (PIC) Modeling of Hall Thrusters," *24th International Electric Propulsion Conference*, Moscow, Russia, 1995, pp. 1213-1224

2.   Parra, F., Ahedo, E., Fife, J., and Martinez-Sanchez, M., "A two-dimensional hybrid model of the Hall thruster discharge*," Journal of applied physics*, Vol. 100, 2006, pp. 023304.

3.   Hofer, R., Mikellides, I., Katz, I., and Goebel, D., "Wall sheath and electron mobility modeling in hybrid-PIC Hall thruster simulations," *AIAA Paper*, Vol. 5267, 2007.

4.  Koo, J. and Boyd, I., "Computational model of a Hall thruster," *Computer physics communications*, Vol. 164, No. 1-3, 2004, pp. 442-447.

5.  Hagelaar, G., Bareilles, J., Garrigues, L., and Boeuf, J., "Two-dimensional model of a stationary plasma thruster," *Journal of applied physics*, Vol. 91, 2002, pp. 5592.

6.  Scharfe, M., Thomas, C., Scharfe, D., Gascon, N., Cappelli, M., and Fernandez, E., "Shear-based model for electron transport in hybrid Hall thruster simulations," *Plasma Science, IEEE Transactions on*, Vol. 36, No. 5, 2008, pp. 2058{2068.

7.  Garrigues, L., Hagelaar, G. J. M., Boeuf, J. P., Raitses, Y., Smirnov, A., and Fisch, N. J., "Two Dimensional Hybrid Model of a Miniaturized Cylindrical Hall Thruster," *30th International Electric Propulsion Conference*, Florence, Italy, 2007, IEPC-2007-157.

8.  Sydorenko, D., Smolyakov, A., Kaganovich, I., and Raitses, Y., "Modification of Electron Velocity Distribution in Bounded Plasmas by Secondary Electron Emission," *IEEE Transactions on Plasma Science*, Vol. 34, No. 3, 2006, pp. 815{824.

9.  Hirakawa, M. and Arakawa, Y., "Particle simulation of plasma phenomena in Hall thrusters," *Proceedings of the 24th International Electric Propulsion Conference*, Moscow, IEPC-95-164, 1995.

10. Szabo, J., Martinez-Sanchez, M., and Batishchev, O., "Fully kinetic Hall thruster modeling," *IEPC Paper*, 2001, pp. 01-341.

11. Fox, J., *Advances in Fully-Kinetic PIC Simulations of a Near-Vacuum Hall Thruster and Other Plasma Systems*, Ph.D. thesis, Massachusetts Institute of Technology, 2007.

12. Sullivan, K., *PIC simulation of SPT Hall thrusters: high power operation and wall effects*, Ph.D. thesis, Massachusetts Institute of Technology, 2004.

13. Raitses, Y. and Fisch, N., "Parametric investigations of a nonconventional Hall thruster," *Physics of Plasmas*, Vol. 8, 2001, pp. 2579.

14. Brieda, L., Keidar, M., Raitses, Y., and Fisch, N., "Self-Consistent Calculation of Electron Transport in a Cylindrical Hall Thruster," *31st International Electric Propulsion Conference*, Ann Arbor, MI, 2009, pp. 1-9.

15. Raitses, Y., Smirnov, A., and Fisch, N., "Effects of enhanced cathode electron emission on Hall thruster operation," *Physics of Plasmas*, Vol. 16, 2009, pp. 057106.

16. Smirnov, A., Raitses, Y., and Fisch, N. J., "Plasma measurements in a 100W cylindrical Hall thruster," *Journal of Applied Physics*, Vol. 95, No. 5, 2004, pp. 2283{2291.

17. Brieda, L., Keidar, M., Raitses, Y., and Fisch, N., "Investigation of Electron Transport in a Cylindrical Hall Thruster using a Kinetic Code," *45th AIAA/ASME/SAE/ASEE Joint Propulsion Conference*, Denver, Colorado, Aug. 2-5, 2009, 2009, pp. 1-8.

18. Wikipedia, "JAVA Performance," `http://en.wikipedia.org/wiki/Java_performance #Compariso_to_other_languages`.

19. Particle In Cell, "Get Results Faster with Java Multithreading," `http://www.particleincell.com/2011/java-multithreading`.

20. Lieberman, M. and Lichtenberg, A., *Principles of plasma discharges and materials processing*, Wiley, 2005.

21. Nicklass, A., Dolg, M., Stoll, H., and Preuss, H., "Ab initio energy-adjusted pseudopotentials for the noble gases Ne through Xe: Calculation of atomic dipole and quadrupole polarizabilities," *Journal of Chemical Physics*, 1995.

22. Szabo Jr, J., *Fully kinetic numerical modeling of a plasma thruster*, Ph.D. thesis, Massachusetts Institute of Technology, 2001

23. Sydorenko, D., *Particle-in-cell simulations of electron dynamics in low pressure discharges with magnetic fields*, Ph.D. thesis, University of Saskatchewan, 2006.

24. 24Brieda, L., Kafafy, R., Pierru, J., and Wang, J., "Development of the Draco code for modeling electric propulsion plume interactions," *40th Joint Propulsion Conference*, Fort Laudardale, FL, USA, 2004

25. Nakles, M., Hargus, W., and VanGilder, D., "Comparison of Numerical and Experimental Near-Field Ion Velocity Distributions of the BHT-200-X3 Hall Thruster," *42nd Joint Propulsion Conference*, Sacramento, CA, 2006, AIAA-2006-4479.

26. Santi, M., Cheng, S., Celik, M., M., M.-S., and J, P., "Further Development and Preliminary Results of the AQUILA Hall Thruster Plume Model," *39th Joint Propulsion Conference*, Huntsville, Alabama, 2003.

# Section 2, Plasma-Wall Interaction in Hall Thrusters with Magnetic Lens Configuration

## Introduction

Hall thrusters are spacecraft propulsion devices that utilize applied magnetic fields and closed electron Hall drift to accelerate quasi-neutral plasma. The typical Hall thruster consists of an annular or cylindrical chamber with one end open to the ambient environment. Neutral propellant is injected through the closed end. This end also contains the anode. An externally located cathode produces electrons, fraction of which enters the chamber and ionizes the propellant. In order to increase the electron transit time, and hence improve the ionization efficiency, a magnetic field is applied over a section of the chamber. This magnetic field restricts the axial motion of electrons, since the electrons become trapped in a closed azimuthal, or Hall, drift about the thruster centerline. The magnetic field thus also plays an important secondary role. Since the motion of electrons is restricted across the field lines, electrons will tend to redistribute radially along the magnetic lines according to the spatial variation in ion density. The magnetic field lines thus become lines of constant potential and an electric field develops in the direction normal to the magnetic field. This electric field accelerates the ionized propellant out of the device.

In the classical Hall thruster, the magnetic field consists primarily of a radial component. Such a configuration appears ideal at first since it produces an electric field with axial orientation. However, the presence of walls modifies the near-wall potential structure and results in a local component accelerating ions into the walls. Ion wall flux contributes to loss of thruster efficiency and to limited thruster lifetime due to channel erosion. In order to mitigate wall losses, some novel Hall thrusters [27,28] have begun experimenting with magnetic fields with convex geometry. Near the walls, this so-called magnetic lens induces an electric field with a radial component directed towards the channel centerline [29]. An interesting aspect of the lens configuration is that in the vicinity of the wall, the resulting magnetic field lines can approach the wall with a highly inclined incidence angle, $\theta$, as measured from the wall normal.

Such a configuration generates an electric field with a strong radial term that, in the case of a sufficiently large $\theta$, dominates the component due to the sheath potential drop [30]. This can be seen from a simple example. Consider a typical 300V Hall thruster with a 200V potential drop occurring across a 1cm wide acceleration zone. The magnitude of the electric field $E_\perp$ is then $2\times10^4$ V/m. Next consider the potential drop due to the wall sheath. The electric field along the magnetic field line in the vicinity of the wall can be estimated from $E_\parallel = T_e\, \partial \ln n / \partial r \sim T_e/\Delta r \sim 20eV/0.01cm \sim 2\times10^5 V/m$ [31]. Here $\Delta r$ is the sheath thickness, which is taken to be 10 Debye lengths. The angle at which the radial component of the electric field becomes negative is given by $E_r = E_\parallel \cos\theta - E_\perp \sin\theta \sim \tan\theta = E_\parallel/E_\perp$, or $\theta \sim 85^o$.

Ions are then accelerated away from the wall and a complete sheath collapse is expected. Although plasma-wall transition has been the subject of much past research, such research typically considered only the generalized radial case [32]. In this paper we investigate the sheath formation and collapse in the presence of a two dimensional magnetic field. The analysis is performed using a 2D particle in cell (PIC) code. We use the code to determine the structure of the plasma sheath for several magnetic field configurations. We first investigate the response of the sheath to an inclined magnetic field. Next we extend the analysis to include the influence of secondary electrons and a magnetic mirror.

We also develop a simple potential solver based on the quasineutral approximation present in standard Hall thruster codes to investigate the effect the field solver has on the sheath solution. We conclude the paper with an analysis of sheath stability, wall flux, and channel erosion.

## Computational Model

### Simulation Domain

We study the sheath formation using a simple axisymmetric electrostatic particle in cell (ES-PIC) code. The code is based on the hybrid approach in which ions are treated as particles, but electrons are represented by a fluid model. The computational domain is limited to a small region near the outer wall, as illustrated in Figure 1. The inset illustrates a hybrid annular/cylindrical Hall thruster, in which the magnetic field geometries of interest can be found. The thruster schematic is based on the Princeton Cylindrical Hall Thruster [27]. The region being studied is also highlighted in the inset. The small size of the domain allows us to resolve the Debye length and thus directly compute the electric potential in a reasonable amount of time (each simulation takes approximately 20 minutes). The domain captures the acceleration region characterized by the presence of the strong applied magnetic field. In our formulation, the anode and the primary ionization zone are located to the left. The upper boundary represents the wall, while the bottom boundary extends into the quasineutral bulk plasma region. Ions are injected into the simulation along the left boundary and leave through the open right and bottom face or by recombining with the upper wall.
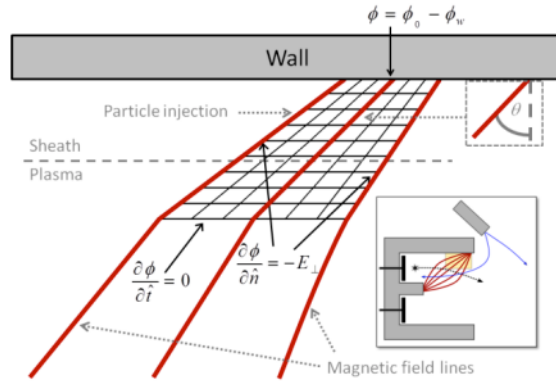


*Figure 1. Schematic of the computational domain. Ion particles are injected from the left. The inset shows a cylindrical Hall thruster and highlights the region analyzed by our code.*

To simplify the subsequent computation, we select a simulation mesh in which the radial gridlines are aligned with the magnetic field. Such a formulation allows us to specify the necessary reference values as a function of the axial grid coordinate only. In constructing the mesh, we paid attention to two requirements. First, the mesh had to be capable of capturing the magnetic topology of interest: varying angle of magnetic field, and also the magnetic mirror effect. Secondly, the mesh had to be suitable from the computational perspective. Particle methods require scattering of particles to the grid nodes, and conversely gathering forces by collecting values from the grid onto particle locations. Topologically structured meshes are preferred here, since physical coordinates can be mapped to the computational space via evaluation of analytical functions. The mesh shown in Figure 1 satisfies both of these requirements. The mesh coordinates are given by

$$r = r_0 + j * \Delta r$$

(1)

$$z = i * \Delta z_j - (nr - 1 - j) * \Delta r * \tan(\theta) - 0.5 * (nz - 1) * \left(\Delta z_j - \Delta z_w\right)$$

where $\Delta z_j$ is the local cell spacing. The cell spacing varies linearly between the top and bottom boundary.

These mesh coordinates can be easily inverted. The $j$ component is obtained first from the radial $r$ coordinate. The $i$ coordinate is then recovered from the axial position $z$ using the second equation.

## Particle Injection

Xenon ions are injected into the simulation domain along the left boundary with initial velocity $u_z = u_0 + u_{th}$. Here $u_0$ is the drift component and $u_{th}$ is a random thermal velocity obtained by sampling

the Maxwellian distribution function at 1eV. The magnitude of the drift component was set to 6 km/s, corresponding to approximately 25eV of upstream acceleration. Initial radial velocity is also obtained by sampling the random thermal component. The number of computational particles injected per time step is obtained from $p = \dot{m}\Delta t / w = n_i \bar{u} A m \Delta t / w$ where $n_i = 5 \times 10^{16}$ m$^{-3}$ is the injection ion density, and $w$ is

the macroparticle weight. The weight was selected such that each cell contained a statistically significant number of particles. Particles are loaded with a zero azimuthal component. We assume that no forces act on ions in the azimuthal direction and hence the cylindrical equations of motion reduce to the Cartesian form. Ion positions are updated at each time step according to the Leapfrog algorithm by integrating the Lorentz force, $\vec{F} = -e\nabla\phi$. The magnetic term is omitted, since in a Hall thruster, ions are not magnetized.

Ions impacting the upper wall or leaving the computational domain are removed from the simulation. Collisions are not included as they generally play only a minor role in the sheath.

## Potential Solver

Potential is computed by solving the Poisson's equation, $\varepsilon_0 \nabla^2 \phi = -e(n_i - n_e - n_s)$, with the

three densities on the right hand side corresponding to ions, primary electrons, and secondary electrons, respectively. Ion density $n_i$ is computed directly by scattering positions of the kinetic ions to the

computational grid. In the frame of reference of ions, electrons respond instantaneously to any disturbance. Electron motion is also not impeded along a magnetic field line. The time-dependent and convective terms on the left hand side of the electron momentum equation then vanish, leaving us only with the force balance [34],

$$0 = e\frac{\partial\phi}{\partial z} - \frac{KT_e}{n_e}\frac{\partial n_e}{\partial z} - \frac{KT_e}{B}\frac{\partial B}{\partial z}$$

(2)

These terms correspond to the electric field, gas pressure, and magnetic field pressures, respectively. This equation can be easily integrated and subsequently inverted to obtain an expression for bulk electron density,

$$n_e = n_0 \frac{B_0}{B} \exp\left[\frac{e}{kT_e}(\phi - \phi_0)\right]$$

(3)

This is the well known Boltzmann relationship modified by the magnetic field strength term. This term is seen to reduce the electron density in regions of an increasing magnetic field – this is the magnetic mirror effect. The standard Boltzmann relationship is recovered if the magnetic field magnitude remains constant along the field lines. It should be noted that Equation 3 holds independently for each magnetic field line. The three constants with the 0 subscript correspond to the reference density, potential, and magnetic field strength. These values are unique and independent along each line. For simplicity, electron temperature is assumed to remain constant, $kT_e = 10\text{eV}$, and there is no variation in magnetic field strength in the axial direction, $\partial B/\partial z = 0$. The reference density is obtained by sampling the ion density along the bottom edge of the simulation domain where $n_i = n_e = n_0$. The reference potential is assumed to decay linearly between the left and right boundaries following $\phi_0 = \phi_L - (20,000\text{V/m})(z_w - z_{w,0})$.

The strength of the magnetic field is computed from the conservation of magnetic flux, $\phi_m = \int_S \vec{B} \cdot \vec{ds}$, or $Br\Delta z = C$, a constant value. Here $\Delta z$ is the cell spacing at the corresponding $r$ value. It should be pointed out that, as indicated by Equation 3, the terms relating to the magnetic strength appear only as a ratio, allowing us to select an arbitrary value for the reference field.

The secondary electron density $n_s$ is obtained from $\nabla \cdot (n\vec{u}) = 0$. Density of secondary electrons at the wall is given by $n_{s,w} = sn_{e,w}$, where $s(T_e, \theta)$ is the SEE yield [31]. In our formulation we assume isotropic angular distribution and energy dependence based on the linear relationship given in [33],

$$s(T_e, \theta) \approx \sigma_0 + (1 - \sigma_0)\frac{E_p}{E_1}$$

(4)

For Boron Nitride, the typical wall material in conventional Hall thrusters, the coefficients $\sigma_0$ and $E_1$ are 0.54 and 40, respectively. $E_p$ is the energy of the incoming particle, measured in eV. Initial velocity of the secondary electrons is taken to be $u_{s,w} = (2kT_w/\pi m_e)^{1/2}$. Energy conservation dictates $u = (2q\Delta\phi/m)^{1/2}$, leading to

$$n_s = sn_{e,w}\left(\frac{kT_w}{e\pi}\frac{1}{\phi - \phi_w}\right)$$

(5)

Boundary Conditions

Potential along the top wall is fixed as $\phi_w = \phi_0 - \Delta\phi_W$, where the wall potential drop is given by [31] as

$$\Delta\phi_w = T_e \ln\left\{\frac{1 - s(T_e, \theta)}{V_{\parallel}\left(\frac{2\pi m}{T_e}\right)}\right\}$$

(6)

The problem is closed by prescribing the normal electric field $E_{\perp}$ along the left and right boundaries, and zero tangential electric field, $E_{\parallel} = 0$ on the bottom boundary. The electric field along the left and right boundaries is non-uniform for cases with a diverging magnetic field line topology. This can be seen from a simple observation of the increasing distance between field lines as one moves away from the wall. The magnitude is obtained numerically by computing the normal distance $d$ to the next magnetic field line (grid line) at each node. The electric field is then set from $E_{\perp} = -\Delta\phi_0/d$. Potential is solved using the finite volume method.

## Quasineutral Solver

In addition to the Poisson solver, we have also implemented an alternative method for obtaining the potential distribution. This approach was developed in order to approximate the solution from Hall thruster codes such as HPHall [35,36]. With the exception of massively parallel fully kinetic programs, codes developed to model Hall thrusters generally do not solve the Poisson's equation. For convergence, Poisson solvers require mesh spacing fine enough to resolve to local Debye length. From the computational perspective, resolving the Debye length is impractical on the spatial scale of a typical thruster. Instead, such codes rely on a simplified quasi one-dimensional approach to solve electron conservation equations in the direction normal to the magnetic field. The axial variation in the reference potential, $\phi_0$, is obtained from the solution of these equations. The radial variation in potential is then computed by assuming quasineutrality, $n_e = n_i$ in conjunction with the thermalized potential model, $\phi = \phi^* + kTe/e \ln(n/n_0)$. This approach is analogous to the formulation used to derive the relationship for bulk electron density, Equation 3. This expression can be inverted to obtain

$$\phi = \phi_0 + \frac{kT_e}{e}\ln\left(\frac{n}{n_0}\frac{B}{B_0}\right)$$

(7)

where $n_e = n_i = n$. Our expression extends the quasineutral formulation by taking into account the varying strength of the magnetic field.

Implementation

Simulations were performed on a domain with 50 cells in the axial and 40 cells in the radial direction. Cell spacing was set to $\sim \lambda_D = 10^{-4}$ m. The simulation time step was adjusted automatically by the code from its initial value of $3 \times 10^{-9}$ s such that ion particles traveled no more than 0.33 cell lengths per time step. The thruster diameter was assumed to be 6 cm. The simulation domain was initially empty of particles and ions were injected into the domain until steady state was achieved. Steady state was characterized by zero net change in particle counts. The simulation then continued for additional 1000 time steps during which results were averaged. The typical number of computational particles at steady state was 700,000. Simulation results, including potential, number densities, particle velocities, and wall fluxes were then exported. A marching squares algorithm was implemented in the code to automatically contour the resulting velocity map to obtain the sheath boundary based. In this work, we assumed that the sheath boundary corresponds to the contour where the radial component of velocity $v = v_B$, the Bohm velocity. The code was implemented in the Java programming language. Simulations were performed on a Dell Precision workstation with eight CPU cores. Each simulation case was launched as an independent thread, and a simple scheduler was implemented to allow concurrent execution of the simulation cases.

## Results

### Potential Distribution at Uniform Density

Often we can obtain useful insight into the solution by considering a simplified case that can be evaluated in a reduced computation time. In our case, we investigated the potential distribution that forms in the presence of a completely uniform plasma. These results are illustrated in Figure 2. In all cases, plasma density of $5 \times 10^{16}$ m$^{-3}$ was used. The contours correspond to the lines of constant potential and the streamtraces visualize the electric field. The classical Hall thruster with a solely radial magnetic field is shown in Figure 2a). As indicated previously, this configuration results in a primarily axial electric field. However, near the wall, the wall potential drop modifies the electric field structure such that the electric field becomes oriented towards the wall. Ions located in this near wall region are then expected to be accelerated to the wall and subsequently lost to the wall recombination. Figure 2b) illustrates what happens when the magnetic field angle is increased to $30^{\circ}$. Increase of the magnetic field incidence angle results in a compression of the region containing the radial electric field. Analogously, the critical streamtrace that delineates the near wall region from the bulk acceleration zone moves closer to the wall. Ions located below this line are expected to be screened from any wall effects and are accelerated in the direction normal to the magnetic field. Ions above this line are lost to the wall.
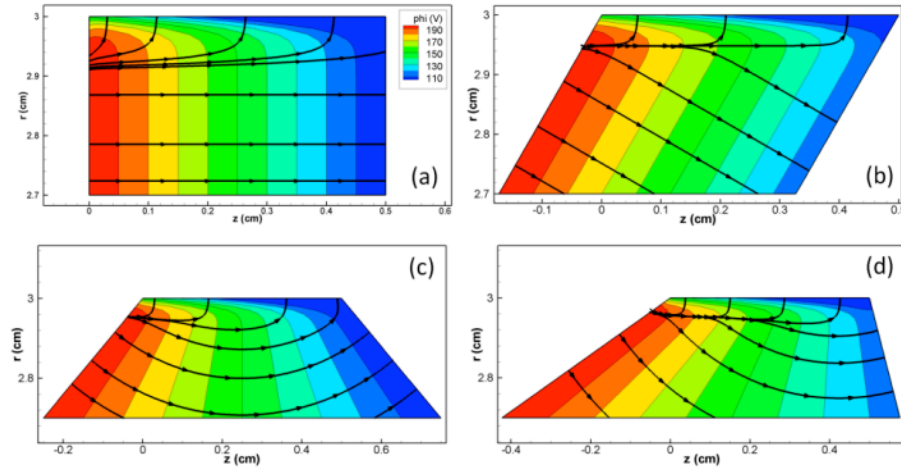
Cases c) and d) show the effect of the magnetic lens. The net angle of the magnetic field is zero in case c), however, the magnetic field strength decreases away from the walls. The magnetic field strength at the bottom edge is $0.5B_w$. The solution is approximately antisymmetric. The electric field is seen to first direct the ions away from the wall in the converging section of the lens. Ions are then accelerated back towards the wall in the diverging section. However, since the field accelerates the ions, the ion velocity will be greater in this half and the diverging effect is expected to be smaller. The predicted result is a net acceleration of ions away from the wall. Case d) extends the magnetic mirror effect in c) by including the 30º field inclination from b). This configuration approximates the magnetic field in thrusters such as the Princeton Cylindrical Hall Thruster. In the CHT, this configuration arises from the difference in the physical location of the inner and outer magnets. Figure 2d) indicates that the effect of combined field divergence and field inclination is a reduction in the defocusing effect seen in c), while at the same time reducing ion wall flux, and retaining the net axial acceleration of ions.

## Sheath variation with magnetic field angle

We build on these initial observations by performing series of plasma simulations. We first investigated the effect of an increasing magnetic field angle in the absence of a magnetic mirror. Secondary electron emission was not included in this set, $s = 0$ in Equation 5. The magnetic field angle $\theta$

increased from 0º (magnetic field normal to the wall) to 85º (highly inclined configuration). Results for 0º, 40 º, 60 º and 70 º are plotted in Figure 3. Ion densities are shown using the contour plot. Velocity streamlines are also plotted, as well as the sheath boundary. The sheath edge corresponds to the contour where the radial velocity component (i.e. component normal to the wall) reaches the Bohm velocity $v_B = \sqrt{kT_e/m_i}$. The sheath edge is plotted by the solid red line. We see that in the case of a zero

magnetic field angle, the solution obtained by our code is similar to the well-known boundary layer problem. The sheath forms short distance from the injection plane and continues to grow as more ions are accelerated from the bulk plasma towards the wall. This result is somewhat non-physical, since in a real device, the sheath thickness will be finite at the entrance to the acceleration zone. Since our simulation resolves only a small subset of the Hall thruster channel, we are unable to capture the sheath that forms upstream of our domain. To investigate the role the initial sheath profile has on results, we tested a modified particle loading algorithm in which we allowed the injection density to decay exponentially towards the wall. We found that differences between the two solutions were limited to several cells near the left boundary. No significant differences in plasma parameters or the sheath profile were observed at downstream locations. This finding can be explained by realizing that any ions injected into the sheath will be rapidly lost to the wall. Hence, we ignore this initial region and characterize the sheath by its maximum thickness.
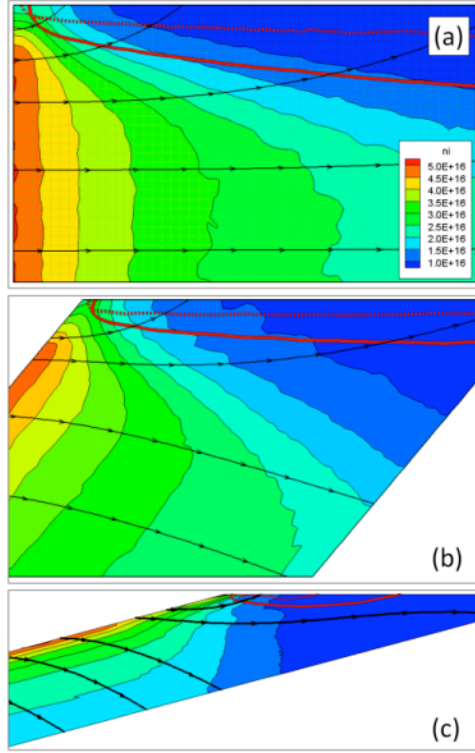
*Figure 3. Simulation results showing the sheath profile for three different magnetic field line angles, $0^o$, $40^o$, and $70^o$, respectively. Streamtraces show ion trajectories. The red lines correspond to the sheath edge as computed with the Poisson solver (solid) and the QN model (dashed line).*

From our simulation we see that the effect of an increasing magnetic field angle is to reduce the sheath thickness, as stipulated in the previous section. At $40^o$, the sheath thickness, as characterized by the ion velocity, asymptotes to a constant thickness. The ion density decays near the wall, however this effect is due to the net acceleration of ions away from the wall by the electric field, and not by the loss of ions to the wall as is the case with the classical sheath model. At $70^o$ we start seeing first evidence of a sheath collapse. The sheath has reduced in axial size and extends only over a small section of the wall. In addition, near the wall, the ion velocity streamlines become parallel to the wall. Ions are thus accelerated along the wall, instead of being attracted into the wall as is the case with a smaller $\theta$.

In this study we also looked at the effect the potential solver plays on the sheath solution. The sheath profile indicated by the dashed red line corresponds to the solution obtained using the simplified quasineutral approach similar. We can see that the sheath thickness is artificially compressed, and extends to approximately three computational cells. For illustration, the computational mesh is displayed in the top figure. The potential solution obtained in the case of a QN solver is completely driven by the local deviation from reference density. Since potential on each node is evaluated independently, the wall potential is artificially screened at a distance equal to one cell length. This is in contrast with the solution from the Poisson solver, which predicts similar screening to occur over distance of several Debye lengths. The QN solution is non-physical, since the magnitude of the near-wall electric field is directly related to the cell spacing. The wall effect in the QN solver is extended to the additional cells by motion of ions, which by their loss to the wall reduce the local density. However, this effect has only a limited capability to communicate the wall potential drop to the bulk plasma. As such, the QN solution results in the wall having a reduced ion-attractive capability compared to the physically-sound Poisson solution. This result is demonstrated in the relative reduction in the sheath thickness.

## Influence of Secondary Electron Emission

We next included secondary electron emission (SEE). Secondary electron emission is an important process in SPT-type Hall thrusters, in which the acceleration channel is lined with an insulator material for which the secondary electron yield can approach unity. SEE may be an important driver in the so-called anomalous electron transport across magnetic field lines. This effect is not investigated in this work. Instead, we only concentrate on the role of SEE on the sheath profile. Same set of cases presented in the previous paragraph was run with the wall potential modified by the presence of SEE. We include secondary electrons in our code by computing the SEE emission coefficient using Equation 4. From the wall potential relationship, Equation 5, we can see that the presence of SEE acts to decrease the sheath potential and hence the sheath thickness. This prediction is confirmed by the result illustrated in Figure 4. This figure shows the potential contours for the $40^o$ magnetic field inclination. The dashed lines correspond to the case with secondary electron emission. Presence of SEE is seen to reduce the sheath thickness, and thus is expected to reduce the flux of ions to the walls.
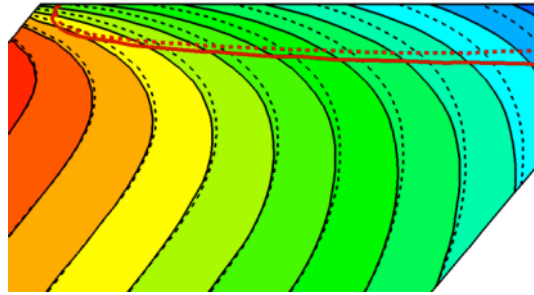


*Figure 4. Potential profile for $40^o$. Dashed lines indicate solution with secondary electron emission.*

## Magnetic Mirror Effect

The final set of simulations was run to investigate the effect of magnetic mirror. We used mirror ratio $B_w$ to $B_0$ of 1.8, and compared case without and with a $40^o$ magnetic field inclination. Here $B_w$ is the field strength at the wall, and $B_0$ is the field at the bottom edge of the simulation domain. We can see from Figure 5 that the mirror plays a role similar to that of the inclined field. As the mirror ratio is increased, the divergence of the field also increases and results in acceleration of ions away from the wall. However, unlike in the case of a uniform magnetic field, the orientation of the electric field past the centerline is reversed, and ions are accelerated towards the wall. This can be seen in Figure 5a), in which ions trajectories that were initially parallel, or leading away from the walls, are seen to turn towards the wall past the field centerline. This outcome is somewhat different that predicted by the case based solely on the magnetic field orientation in Figure 2c). We see that the presence of ions, and hence non-uniform plasma density, results in the sheath forming normal to the magnetic field lines, instead of parallel to the wall as was the case in Figure 2. Figure 5b) plots the solution obtained by including a $40^o$ magnetic field inclination. Ions are again seen to be initially accelerated away from the wall. However, past the centerline the electric field becomes oriented axially, acting to accelerate ions along the thruster centerline. This net axial acceleration reduces flux of ions to the wall and reduces the sheath thickness.
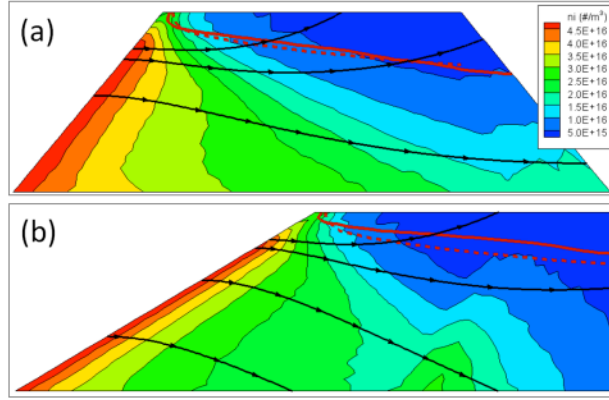
*Figure 5. Ion density contours in the presence of magnetic mirror. Magnetic mirror strength of 2 is used in both cases. Case (b) includes a 40° magnetic field inclination.*

## Discussion

### Sheath Collapse

In Figure 6 we plot the variation in maximum sheath thickness with the incidence magnetic field angle. We consider three cases: inclined magnetic field, inclined magnetic field with a magnetic mirror and SEE, and an inclined field solved using the quasineutral potential solver. We see that in all cases the sheath thickness decreases as the magnetic field incidence angle is increased. Figure 3 shows that at 70° the sheath surrounds only a small portion of the wall. From Figure 5 we also see that the sheath has reduced in maximum thickness by 80% from the value obtained at 0°. The sheath thickness obtained in the presence of magnetic mirror closely follows the trend of pure field inclination. The slight increase in the thickness with the mirror may be due to the increase of the domain size associated with the diverging field. Of greater interest is the solution obtained using the QN approach. This resulted is plotted used the dashed line. We can see that the QN method under-predicts the sheath thickness by a factor of 3. In addition, the QN approach also results in a much smaller dependence of sheath thickness on the applied magnetic field angle. This result indicates that the quasineutral formulation used in typical Hall thruster codes may not be a good candidate for determine wall fluxes, and additional steps should be taken to correct the wall ion flux[37].
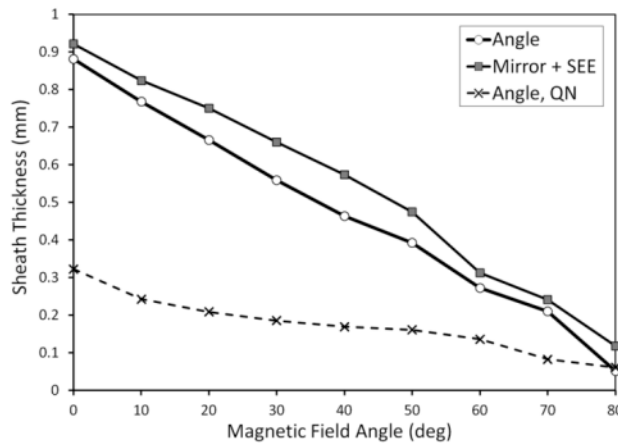


*Figure 6. Variation of maximum sheath thickness with the angle of magnetic field. Dashed line corresponds to the solution obtained assuming quasineutrality.*

The sheath is seen to collapse at angles greater than 80$^\circ$, confirming the simple analysis presented in the introduction. To better illustrate the dynamics at this highly inclined magnetic field geometry, we plot ion velocity contours and velocity streamlines at the 85$^\circ$ incidence angle. This resulted is shown in Figure 7. The contour plot corresponds to the radial velocity component normalized by the Bohm speed. We can see that at this high incidence angle, the radial component of ion velocity never reaches the Bohm speed. In addition, ions are moving towards the wall only along a small region near the left boundary. This result is likely a direct byproduct of our loading scheme since it affects only the ions injected into the sheath. Ions in the bulk plasma region are instead accelerated away from the wall. Ions located just a small distance from the wall are seen to follow trajectory first parallel to the wall, and subsequently turning away from the wall. Ions are thus seen to be repelled by the wall, indicating a full sheath collapse.
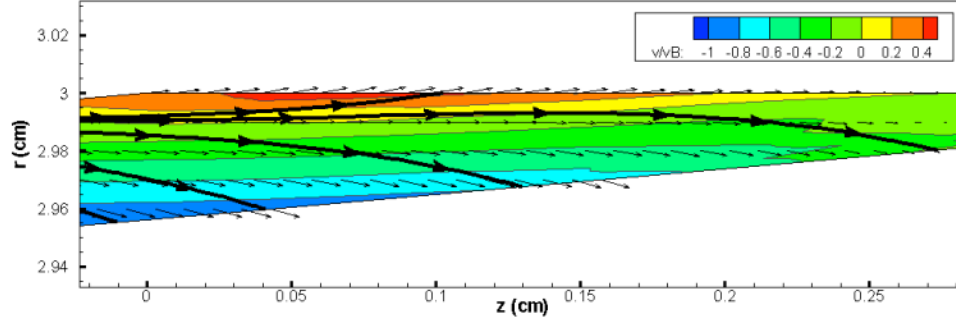


Figure 7. Plots of normalized radial velocity and ion velocity streamlines at θ=85$^o$.

## Erosion and Lifetime

Our numerical results confirm that the presence of highly inclined magnetic fields results in a decreased flux of ions to the wall, and eventually a sheath collapse. This observation has a profound effect on both the ionization efficiency and the thruster lifetime, since ion losses to the walls are a major contributor to both of these inefficiencies. Here we consider only the wall erosion. Material sputtering yield scales with both the impact angle and the energy of the incoming ions. Several models exist for computing sputter yields for Boron Nitride, the material typically used in SPT-type Hall thrusters. In this work we utilize the logarithmic fit suggested by Garnier [38],

$$Y_0(E) = 0.0156 \ln E - 0.0638 \tag{8}$$

This fit is valid from the energy threshold of 60 eV up to keV. In our analysis we neglect low energy sputtering. For angular dependence of yield, quadratic polynomial fit is recommended by Yim [39].

$$Y(E,\theta) = Y_0[-4.45 \times 10^{-7}\theta^4 + 4.91 \times 10^{-5}\theta^3 - 9.72 \times 10^{-4}\theta^2 + 3.44 \times 10^{-3}\theta + 1] \tag{9}$$

where θ is in degrees.

Figure 8 shows the computed wall flux and sputter yields for several representative cases. The baseline is the configuration with normal radial field, no SEE, and no magnetic mirror. Addition of secondary electrons is seen to reduce the wall flux, although the effect is small. Greater difference is observed in the calculated sputter yield. Since the presence of SEE reduces the wall potential drop, impacting ions will possess lower energy and hence the total erosion rate will decrease even if the flux remained the same. A much greater effect is seen when the magnetic field angle is increased to 40$^\circ$. Flux reduces by approximately 60%, leading to a correspondingly similar reduction in erosion rate. Inclusion

of the magnetic mirror effect (at $B_w/B_0$=1.8) reduces the flux even further, although the effect is not as pronounced as due to the magnetic field inclination.
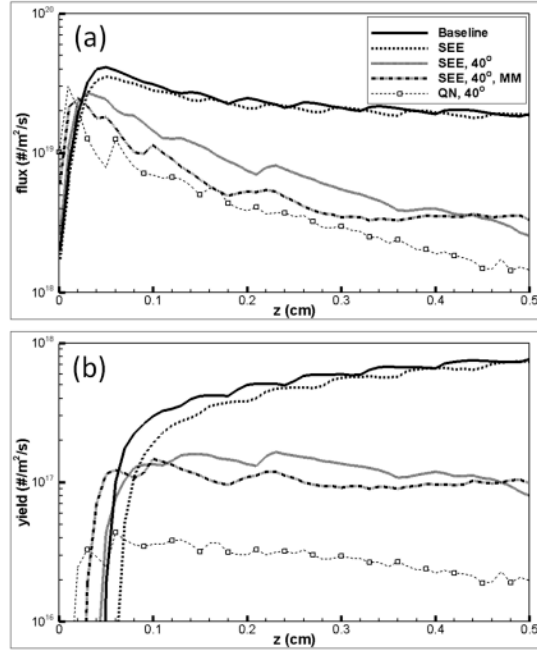


*Figure 8. Comparison of wall flux and computed sputtered yield for 5 selected configurations.*

The dashed line with markers corresponds to a 40° incidence angle and the quasineutral field solver. This case thus corresponds to the solution plotted with the dotted line, SEE and 40°. We can see that although the QN solver produces trend qualitatively comparable to the reference case, the computed fluxes and yields do not agree quantitatively. Average QN flux is $3.5\times10^{18}$ #/m²/s compared to $7.2\times10^{18}$ #/m²/s obtained using the Poisson solver. This difference corresponds to a 50% numerical reduction in wall flux. Comparably, the average sputter yield decreases from $1.5\times10^{17}$ #/m²/s to $3.1\times10^{16}$ #/m²/s with the QN solver, corresponding to an 80% decrease. The QN method for obtaining potential is seen to both decrease the wall flux, and also decrease the energy of the impacting ions, underpredicting the erosion rates by almost one order of magnitude.

**Sheath Stability**

The analysis presented in the previous paragraphs was performed using the prescribed normal component of electric field $E_\perp = 20 \text{ kV/m}$. The electric field magnitude is a design parameter of the

thruster, as it is arises from the particular design of the magnetic circuit and also the potential drop between the cathode and the anode. To investigate the effect the field strength has on the sheath profile, we ran the code for several values of $E_\perp$ with $\theta$=60°, no SEE, and no magnetic mirror. These results are

plotted in Figure 9. The solid line at 20kV/m corresponds the case shown previously. Reducing the applied potential drop leads to a thicker sheath, as expected. We can see that for this particular case, full sheath collapse will occur approximately at $E_\perp = 50 \text{ kV/m}$. It should be pointed out that this model

predicts that the inclined magnetic field leads to sheath formation only if axial electric field is small. According to this model it is predicted that the potential drop inside the Hall thruster channel decreases leading to shifting the potential drop outside. Such effect has significant implications on the plume formation and the thruster contamination aspects. It is interesting to point out that such trend is also observed experimentally[40,41,42].
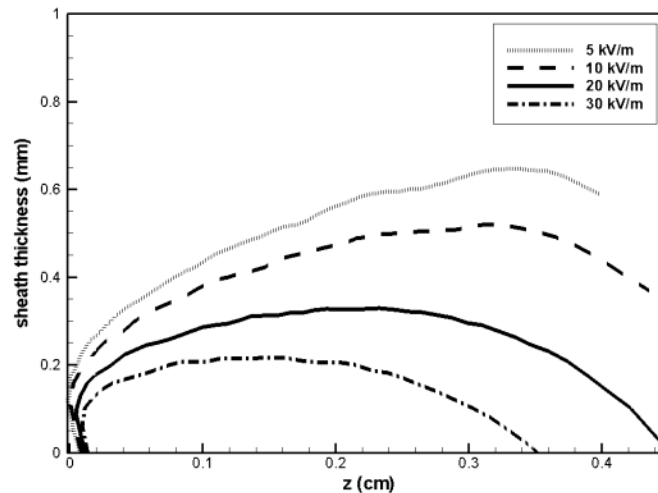


*Figure 9. Sheath profile for $\theta=60^o$ as a function of normal electric field*

## Conclusion

In this paper we investigated the topology of the plasma sheath that forms along the wall in the acceleration zone of a Hall thruster in the presence of a two dimensional magnetic field. Our analysis concentrated on the effect an increasing angle of magnetic field incidence plays on the maximum sheath thickness. It was shown that at highly inclined angles, ions are repelled by the wall and the sheath collapses. In addition, we studied the effect of secondary electron emission and magnetic mirror. Both of these processes reduced wall fluxes, however, the effect was negligible compared to the effect obtained purely by the increased magnetic field incidence angle. We used the computed wall fluxes along with an erosion fit to predict the effect the magnetic field topology has on thruster lifetime. The erosion rate was seen to decrease by almost one order of magnitude with increase of the incident field to $40^o$. In addition, we compared our results to those obtained by typical Hall thruster codes that utilize simplified quasineutral approach to obtain the radial electric field. We found that the QN approach is not suitable for determining wall fluxes and erosion rates, as the computed results underpredicted the results obtained by the more physically accurate Poisson solver by almost one order of magnitude.

## References

27.     Raitses, Y., and Fisch, N.J., "Parametric investigation of a nonconventional Hall thruster," *Physics of Plasmas,* vol. 8, pp. 2579, 2001

28.     Reid, B.M., and Gallimore, A.D., "Plasma Potential Measurements in the Discharge Channel of a 6-kW Hall Thruster," *44th AIAA Joint Propulsion Conference,* Hartford, CT, 2008

29.     Fruchtman, A., and Cohen-Zur, A., "Plasma lens and plume divergence in the Hall thruster", *Applied Physics Letters*, Vol. 89, pp 111501, 2006

30.     Keidar, M., and Beilis, I.I., "Sheath and boundary conditions for plasma simulations of a Hall thruster," *Applied Physics Letters*, Vol. 94, pp 191501, 2009

31.     Keidar, M., Boyd, I.D., and Beilis, I.I., "Plasma flow and plasma-wall transition in Hall thruster channel", *Physics of Plasmas*, Vol. 8, pp. 5315, 2001

32.     Sydorenko, D., Smolyakov, A., Kaganovic, I., and Raitses, Y., "Kinetic simulation of secondary electron emission effects in Hall thrusters," *Physics of Plasmas,* Vol. 13, pp 014501, 2006

33.     Dunaevsky, A., Raitses, Y., and Fisch, N.J., "Secondary Electron Emission from Dielectric Materials of a Hall Thruster with Segmented Electrodes," *Physics of Plasmas*, Vol. 10, pp 2574, 2003

34.     Keidar, M., and Boyd, I.D, "On the Magnetic Effect in Hall Thrusters," *Applied Physics Letters*, Vol. 87, pp 121501, 2005

35.     Fife, J.M., "Two-Dimensional Hybrid Particle-In-Cell (PIC) Modeling of Hall Thrusters," *24th International Electric Propulsion Conference*, Moscow, Russia, 1996

36.     Parra, F.I., Ahedo, E., Fife, J.M., and Martinez-Sanchez, M., "A two-dimensional hybrid model of the Hall thruster discharge", *Journal of Applied Physics*, Vol. 100, pp 023304, 2006

37.     Parra, F.I., and Ahedo, E., "Fulfillment of the Bohm condition on the 'HPHall' fluid-PIC code", *40th Joint Propulsion Conference*, Fort Lauderdale, FL, 2004

38.     Garnier, Y. Viel, V., Roussel, J.F., and Bernard, J., "Low-energy xenon ion sputtering of ceramics investigated for stationary plasma thrusters," *Journal of Vacuum Science & Technology A*, Vol. 17, pp. 3246, 1999

39.     Yim, J.T., Keidar, M., and Boyd, I.D., "A hydrodynamic-based erosion model for Hall thrusters," *29th International Electric Propulsion Conference*, Princeton, NJ, 2005

40.     Raitses, Y., Staack, D., Keidar, M., and Fisch, N.J., "Electron-wall interaction in Hall Thrusters," *Physics of Plasmas*, Vol. 12, pp. 057104, 2005

41.     Linnell, J.A., and Gallimore, A. D., "Internal plasma potential measurements of a Hall thruster using plasma lens focusing,", *Physics of Plasmas*, Vol. 13, pp. 103504, 2006

42.     Raitses, Y., Smirnov, A. and Fisch N.J., "Effects of enhanced cathode electron emission on Hall thruster operation," *Physics of Plasmas*, Vol. 16, pp. 057106, 2009

## Relevance/Transitions

One graduate Ph.D student, Lubos Brieda was involved in this project. He is expected to obtain Ph.D degree at the George Washington University in Spring 2012.

## Acknowledgment / Disclaimer

## Publications resulted from the project:

### Journal papers:

L. Brieda, S. Pai, and M. Keidar, Kinetic Analysis of Electron Transport in a Cylindrical Hall Thruster, *IEEE Transaction on Plasma Science*, Vol. 39, No.11, 2011, pp. 2946-2947.

L. Brieda, and M. Keidar, Plasma-Wall Interaction in Hall Thrusters with Magnetic Lens Configuration, *J. Applied Physics*, under review.

### Conference Papers:

Lubos Brieda, Shaunak Pai, Yitzy Dachman, and Michael Keidar, Wall Interaction in Hall thrusters with Magnetic Lens Configuration, 47th AIAA/ASME/SAE/ASEE Joint Propulsion Conference, San Diego CA, July 29-Aug. 3, 2011.

L. Brieda and M. Keidar, Multiscale modeling of Hall thrusters, 32nd International Electric Propulsion Conference in Wiesbaden, Germany, Sept. 11-15 2011, Paper IEPC-2011-101.